University of Bristol - Explore Bristol Research
General rights

Aeroelastic Tailoring of a Representative Wing-Box Using Tow-Steered Composites

O. Stodieck [1], J. E. Cooper[2], P. M. Weaver[3]

Department of Aerospace Engineering, University of Bristol, Bristol BS8 1TR, U.K.

and

P. Kealy[4]

Airbus Operations UK Ltd, Filton, Bristol BS99 7AR , U.K.

There has been an increasing effort to improve aircraft performance through using composite tailored structures, not only to reduce weight, but to exploit beneficial aeroelastic couplings. Recent work has considered the ability to tow-steer the composite plies in order to achieve better performance. Here, we assess the potential wing weight savings of a full size aeroelastically tailored wing, by optimizing the properties of a three-dimensional finite element model using straight fiber and tow-steered composites in the skins. One and two-dimensional thickness and laminate rotation angle variations are considered as design freedoms. The jig shape is updated to maintain a fixed 1g flight shape and optimization constraints are implemented on the strains and buckling loads due to maneuver and dynamic gust loads, he flutter stability and the control effectiveness for different flight conditions. The optimal main fiber direction is rotated forward of the front spar direction in the outer wing, leading to extension-shear coupling in the skins, which increases the wash-out behavior of the wing. Wash-out effects shift the lift forces inboard and allow skin thickness reductions, but also lead to reductions in aileron control effectiveness. The optimized tow-steered laminate configurations achieved larger mass reductions than optimized straight fiber configurations.

Nomenclature

b	Wing span
$\boldsymbol{B_{hh}}$	Structural modal damping matrix
c	Wing chord
$\boldsymbol{d}$	Wing shape at design 1g flight point

---

[1] Aerospace Engineering Research Assistant
[2] Royal Academy of Engineering Airbus Sir George White Professor of Aerospace Engineering, AFAIAA
[3] Professor in Lightweight Structures
[4] Loads and Aeroelastics Engineer

$f(j)$	Jig shape error function
$\overline{F}, F(j, K)$	Internal loads due to 1g rigid and flexible trim respectively at the design flight point
F_g	Flight profile alleviation factor
g	Artificial structural damping term
H	Gust gradient distance
j	Wing jig shape
k	Reduced frequency
$|k|$	Fiber curvature
K, K_{hh}	Stiffness and modal stiffness matrices
K_d	Differential stiffness matrix
M	Mach number
M, M_{hh}	Mass and modal mass matrices
M_{wing}	Wing structure mass
MLW	Maximum landing weight
MTOW	Maximum take-off weight
MZFW	Maximum zero fuel weight
P	Vector of user specified applied discrete or gust loads
$\bar{q}$	Dynamic pressure
Q_{hh}^I, Q_{hh}^R	Modal aerodynamic damping and stiffness matrices
Q_a, Q_x	Aerodynamic influence coefficient matrices
$\|\nabla t\|$	Skin thickness gradient
$t_{L,U}$	Lower and upper wing skin thickness
$u_a, \ddot{u}_a$	Wing nodal deflections and accelerations
u_x	Vector of extra aerodynamic points
u_h	Vector of modal participation factors
U, U_{ref}	Peak and reference gust velocities
V	Aircraft velocity
w_g	Gust velocity experienced by the aircraft in the time domain
x, y, z	Global coordinate system, with x in the streamwise direction, y in the spanwise direction

Z_{mo}	Maximum operating altitude
β	Aileron deflection angle
ε	Maximum absolute principal strain
$\theta_{L,U}$	Lower and upper wing skin laminate rotation angle
λ_h	Eigenvalue of the flutter problem
λ_n	Buckling reserve factors
ξ_h	Damping ratio
$\boldsymbol{\phi_n}$	Buckling eigenvector
$\dot{\phi}$	Aircraft roll rate
ω_h	Circular vibration frequency
$\mathfrak{I}$	Aileron control effectiveness

I.   Introduction

In flight, the aerodynamic loads on an aircraft wing are not only a function of the aircraft's speed, altitude and accelerations, but also of the wing's static deflections under load and its dynamic behavior. As important background information it is useful to define aeroelasticity [1] as the discipline studying the ensuing interactions of the aerodynamic, elastic and inertial forces. The wing's aeroelastic behavior not only determines the wing loads, and therefore the internal structural stresses and deflections, but also the airspeeds where flutter or divergence instabilities may occur and also the extent to which the wing mounted control surfaces remain effective at high airspeeds.

The aeroelastic tailoring of forward-swept composite wings was first proposed in 1975 by Krone [2]. In the 1980s, it was demonstrated on the X-29 experimental aircraft, where a wash-out effect (wing up-bend coupled to nose-down twist) was used to increase the divergence speed of the forward-swept wing [3]. Since then, it has been shown that the application of aeroelastic tailoring may lead to significant overall aircraft performance improvements in terms of reduced weight, reduced drag, reduced aerodynamic gust loads and higher flutter/divergence instability airspeeds [4-9], by concurrently optimizing the structural and aerodynamic behaviors. The improvement in wing static and/or dynamic behavior in different airflows is typically achieved by adjusting the wing stiffness and the coupling between wing bending and torsion deformations.

Aerospace composites are often stacked homogeneously to provide specially orthotropic laminates, with 0°/±45°/90° angle unidirectional plies. Using these types of laminates, the stiffness of a wing component such as

a wing skin, is a function of the zero-degree ply angle relative to the wing component, as well as the proportion of 0°/±45°/90° plies, their stacking sequence and the total laminate thickness. In order to change the stiffness within a component, it is necessary to add or drop plies, which introduces load offsets and fiber discontinuities leading to stress concentrations that can reduce the strength of a laminate. The rate of ply drops is therefore usually constrained [10], such that stiffness changes can only be very gradual over a part, which may reduce the design space available with traditional laminates in terms of aeroelastic tailoring.

An alternative configuration to the traditional straight-fiber laminates considers the so called 'variable stiffness' or 'variable angle tow' (VAT) or 'tow-steered' laminates, where the fiber angles vary continuously in the plane of the ply. It has been shown that VAT laminates can be used to increase the buckling loads [11-14] or reduce the stress concentrations around structural discontinuities [15, 16]. VAT laminates may be manufactured using different tow-steering methods, such as automatic fiber placement (AFP), tailored fiber placement (TFP) and continuous tow sheering (CTS) [17]. Lately, there has also been an interest in understanding the potential benefits of VAT laminates in terms of aeroelastic tailoring. Recent work on beam and plate models [18-20] showed some benefits of VAT laminates in terms of reducing trim and gust loads and increasing flutter velocities compared to equivalent straight fiber configurations. Stanford et al [21] then used tow-steering to optimize the more realistic wing-box of the NASA Common Research Model (CRM), which is also used for this study. Tow-steering was shown to reduce the wing mass compared to straight fiber configurations by up to 6% under maneuver load and flutter constraints. Brooks et al [22] also recently used a coupled Finite Element Method (FEM)/ Computational Fluid Dynamics (CFD) framework to optimize a high aspect ratio wing for maneuver loads and found that tow-steering was able to decrease the wing mass by 13%. However, these studies did not consider dynamic gust loads or control effectiveness constraints. Indeed, Kenway et al [23] showed that the dynamic gust loads may become critical if the design is only optimized for maneuver cases. Up until the present time, mainly one-dimensional (spanwise) tow-steering have been considered. Although Brooks et al [22] presented results for a two-dimensional fiber angle variation in the skins, no comparisons were made with spanwise (one-dimensional) optimizations, leaving the potential benefits unclear.

In this study, a representative three-dimensional wing-box model is aeroelastically tailored using both straight fiber and tow-steered laminates in the skins. Our aim is to consider the effect of not just maneuver load cases and flutter constraints, as done previously, but also dynamic gust load cases and control effectiveness. Moreover, the effect of increasing the dimensionality of the thickness and fiber angle variations is assessed in this study by considering one and two-dimensional variable distributions, assuming a locally homogenized orthotropic

constant-ply-percentage laminate. The 1g shape of the wing is fixed so as to maintain the aerodynamic cruise performance of the wing. In this case, the performance of the aircraft may be considered to be inversely proportional to the mass of the wing structure, which is minimized for all of our optimization studies. Buckling and maximum strain constraints for realistic maneuver and gust load cases are implemented, with additional flutter/divergence and control effectiveness constraints. Manufacturing considerations in terms of the maximum thickness gradient and maximum fiber curvature are included as constraints. For the optimization studies, linear aeroelastic analyses using MSC NASTRAN are coupled to the Globally Convergent Method of Moving Asymptotes (GCMMA) [24] gradient based optimizer. Beyond structural mass comparisons for different configurations, our aim is to identify those physical behaviors and constraints that drive the design configurations. In line with this goal, optimizations with either only maneuver, gust, flutter or control effectiveness constraints are also performed. Graphical representations of the flexural axis along the wing are used to compare the configurations in terms of effective bend-twist coupling and to further inform understanding of our results. We introduce modelling and optimization approaches first (sections II and III), before analyzing optimization results for one and two-dimensional variable distributions (sections IV and V).

II.   Model description

The half-wing FEM model, shown in Figure 1, is based on the NASA Common Research Model (CRM) [25], which is representative of a long-range commercial aircraft wing-box with a half-span of 29.4m, a quarter-chord sweep angle of 35° and an aspect-ratio of 9. The reference geometry is taken from [26] and corresponds to the 1g flight shape. The wing-box consists of 2 spars, 27 ribs and top and bottom covers with 6 stringers each, which is consistent with the number of ribs and stringers used in reference [21], but which results in a very wide stringer spacing compared to reference designs, where the number of stringers per skin is closer to 30. This implies that the skins in this model carry more loads and have less support against buckling deflections than in a typical design. The reduced number of stringers is therefore likely to result in excessively low panel buckling loads, but it may also have a beneficial effect from an aeroelastic tailoring point of view, since it reduces the effect of the stringer orientation on the main stiffness direction and on the shear-extension stiffness coupling of the skins.

The wing structure is modelled in 3D, using shell elements for the skins, ribs and spars and beam elements for the stringers. The addition of a rigid fuselage and horizontal tailplane (HTP) allows symmetric trim load cases to be analyzed. Discrete mass elements are used to model the wing fuel (42300kg max), leading and trailing edge

devices (1200kg, 2500kg), the engine (5200kg) and the residual structure and payload (63800kg), leading to an aircraft maximum take-off weight (MTOW) of 248200kg, assuming a half-wing structure mass of 9100kg.

The aerodynamic loads are calculated using the doublet-lattice method (DLM) implemented in MSC NASTRAN [27], and the corresponding doublet lattice mesh is also shown in Figure 1. A surface spline is used to transfer the aerodynamic loads to the structure and to update the doublet-lattice mesh with the deflections of the structure, such that aeroelastic effects due to the flexibility of the wing are considered. In order to improve the loads and flutter estimation in the transonic region, CFD-generated aerodynamic influence coefficients are used to update the doublet-lattice aerodynamics. All analyses use linear structural assumptions and are performed in MSC NASTRAN on a single 16 CPU node (2.6GHz CPUs with 4GB RAM/CPU), running analyses in parallel where possible. The following sub-sections detail each type of analysis performed.
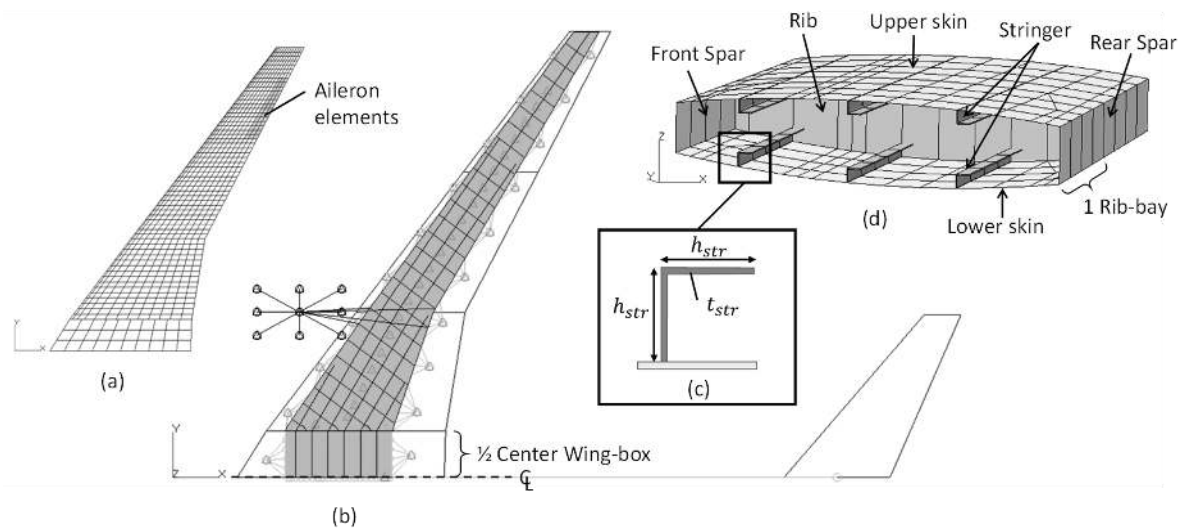

Figure 1 – a) Wing DLM mesh, b) Half-wing trim model with overlay of the FEM (filled with outline of stringers and rib positions) and DLM (black outer outline), including non-structural mass elements (triangles), the rigid HTP and fuselage, c) L-stringer section dimensions, d) Typical wing section and FEM mesh

A.   Jig shape calculation

The jig shape (j) corresponds to the shape of the unloaded wing, which is designed so that the wing takes up its desired shape in flight. For this study, the jig shape was assumed to be a function of the input 1g flight shape (d) and of the stiffness of the wing (K) only. During optimization studies, the jig shape FEM nodal locations are re-calculated for every stiffness update of the wing using an iterative quasi-newton method, which is numerically inexpensive and simple to implement. The initial jig shape (j_0) estimate is the deflected shape of the 1g shape wing with the negative values of 1g rigid trim loads ($\overline{F}$) applied, effectively assuming $j_0 = d - K^{-1}\overline{F}$. The subsequent jig shape iterations are found using

$$f(j) = j + K^{-1}F(j, K) - d$$

$$f'(j) = 1 + K^{-1}\frac{\partial F(j, K)}{\partial j} \approx 1 \tag{1}$$

$$j_{n+1} = j_n - \alpha_n \frac{f(j_n)}{f'(j_n)} = j_n - \alpha_n[j_n + K^{-1}F(j_n, K) - d]$$

where $F(j, K)$ are the FEM internal loads due to 1g trimmed flight at the design flight point (36000ft and M=0.85, with half the MTOW fuel in the outer wing) and α_n is a relaxation parameter, updated based on the jig shape convergence history. In most cases, the initial guess was found to be close to the converged solution, as the 1g tip deflection is small compared to the wing half-span (<<10%) and the assumption $\partial F(j, K)/\partial j \approx 0$ was therefore verified. Generally, the jig shape calculation converged within 2 or 3 iterations, although, in some cases, the error function $f(j)$ converged towards small non-zero values (up to 3mm error) due to local displacement errors near stringer runouts and engine load input locations. These local errors were not found to have a significant effect on the 1g lift distribution. It should be noted that, for very flexible wings, the convergence may be improved by approximating the load derivatives $\partial F(j, K)/\partial j$ using additional function evaluations and a secant method, such as Broyden's method [28].

B.   Symmetric maneuver analysis

Symmetric 2.5g and -1g maneuvers are generally considered to represent critical load cases for sizing of the wing skins. The symmetric maneuver loads are applied to the jig shape wing so as to capture the deflections of the wing accurately. The analyses assume a quasi-static trim condition of the flexible wing, such that

$$[K - \bar{q}Q_a]\,u_a + \ddot{u}_a = \bar{q}\,Q_x\,u_x + P \tag{2}$$

where K and M are the structural stiffness and mass matrices respectively, $\bar{q}$ the dynamic pressure ($\frac{1}{2}\rho V^2$), Q_a and Q_x the aerodynamic influence coefficient matrices used to calculate the aerodynamic forces for the wing and horizontal tailplane (HTP) respectively, and P the vector of user specified applied loads (e.g. engine thrust). The vectors u_a and $\ddot{u}_a$ are the wing nodal deflections and accelerations and u_x is the vector of extra aerodynamic points used to describe the HTP deflections and the rigid body motions, including the input vertical trim accelerations. Once the wing deflections u_a are determined using equation (2), the internal loads and strains at all element are recovered.

A linear buckling analysis is then performed in MSC NASTRAN using the internal loads from the trim analysis as inputs. The buckling reserve factors, i.e. the ratios of the buckling loads to the applied trim load, are the eigenvalues λ_n of the buckling eigenvalue problem

$$K\boldsymbol{\phi}_n + \lambda_n K_d \boldsymbol{\phi}_n = 0 \tag{3}$$

where K is the structural stiffness matrix as before, K_d is the differential stiffness matrix and $\boldsymbol{\phi}_n$ the buckling eigenvector. The lowest 10 buckling reserve factors are calculated and an empirical factor of $1/1.7$ applied based on the comparison between the buckling load of the current FEM mesh and an eight times refined mesh. Although the refined mesh buckling analysis could have been directly included in the optimization study, significantly longer optimization run times (CPU time refined = 400s, coarse=22s) would have ensued. The results in section (IV.A) confirm that the buckling load estimates are conservative. More accurate buckling estimates could have been obtained using a sub-modelling or sub-structuring approach, where a refined mesh or analytical buckling analysis is performed at the rib bay or panel level, using the loads from the full wing model. Such methods could be implemented in future studies, but they do not constitute the main focus of the current study.

C.   Flutter and divergence analysis

It is noted that flutter is a dynamic aeroelastic behavior where the wing structure extracts energy from the airflow, resulting in self-excited vibrations. On the other hand, divergence is a static aeroelastic effect, where the increase in structural elastic forces is overcome by the increase in aerodynamic forces with increasing wing deflections. Both types of behavior can lead to potentially catastrophic failure of the airframe and should therefore be considered early in the design process. The basic expression for modal flutter analysis using the PK-method [27] is

$$\left[M_{hh}\lambda_h{}^2 + (B_{hh} - \frac{\bar{q}}{2V} c Q_{hh}^I / k)\lambda_h + \left(K_{hh} - \bar{q} Q_{hh}^R \right) \right] u_h = 0 \tag{4}$$

where M_{hh} is the modal mass matrix, B_{hh} the modal damping matrix, K_{hh} the modal stiffness, Q_{hh}^I the modal aerodynamic damping matrix and Q_{hh}^R the modal aerodynamic stiffness matrix (functions of Mach number M and the reduced frequency $k = \omega_h c/(2V)$), λ_h is an eigenvalue of the system ($\lambda_h = \omega_h(-\xi_h \pm i\sqrt{1 - \xi_h^2})$), and u_h is a vector of modal participation factors. The system is solved iteratively, using a frequency matching approach, because both the aerodynamic forces and the eigenvalues are a function of the circular vibration frequency ω_h. Eigenvalues with positive real parts (damping ratio $\xi_h < 0$) and non-zero imaginary parts indicate a flutter

instability has occurred, whereas eigenvalues with positive real parts and zero imaginary parts indicate divergence has occurred. The analyses are performed on the half-wing 1g shape model, which includes the HTP and is free at the wing root to move in the vertical direction and to rotate about the pitch axis, so that only symmetric flutter modes are calculated including the effects of rigid-body contributions.

D.   Discrete gust analysis

For this study, the discrete gust cases defined in the certification requirements [29] are used. The aircraft is considered to be in level 1g flight when it encounters a symmetric vertical (1-cos) gust, defined in terms of the peak gust velocity U as

$$U = U_{ref} F_g \left(\frac{H}{350}\right)^{1/6}$$

(5)

where U_{ref} is a linear function of altitude, varying linearly from 17.07m/s (56ft/s) equivalent airspeed (EAS) at sea level to 13.41m/s (44ft/s) EAS at 4572m (15000ft), and to 6.36m/s (20.86ft/s) EAS at 18288m (60000ft), F_g is a flight profile alleviation factor and H is the gust gradient distance in feet (equal to half the gust length), with 10 gust gradients varying between 9m (30ft) and 107m (350ft) analysed for each flight point. F_g is increased linearly from the sea level value

$$F_g = 0.5 \left(1 - \frac{Z_{mo}}{250000} + \sqrt{\frac{MZFW}{MTOW} \tan\left(\frac{\pi \, MLW}{4 \, MTOW}\right)}\right)$$

(6)

to a value of 1 at the cruise altitude (36000ft), where Z_{mo} is the maximum operating altitude (43000ft), MZFW the maximum zero fuel weight (160300kg), MTOW the maximum take-off weight (248200kg) and MLW the maximum landing weight (196300kg), as per CS-25.341 [29]. The effective gust experienced by the aircraft flying at velocity V (TAS) is then described in the time domain as

$$w_g(t) = \frac{U}{2}\left(1 - cos\left(\frac{2\pi V t}{2H}\right)\right)$$

(7)

The applied transient gust load is transformed into the frequency domain using the Fast Fourier transform technique. The dynamic aeroelastic equation is similar to equation (4), except that the K-method formulation for the aerodynamic terms is used, including the artificial structural damping term g, and with the null right-hand term replaced with the applied gust loads $P(\omega)$, such that the system equation becomes

$$[-\boldsymbol{M}_{hh}\omega_h{}^2 + i\boldsymbol{B}_{hh}\omega_h + (1+ig)\boldsymbol{K}_{hh} - \bar{q}\boldsymbol{Q}_{hh}]\boldsymbol{u}_h = \boldsymbol{P}(\omega) \tag{8}$$

This system of equations is subsequently solved in the frequency domain and the transient gust response, including the wing deflections, internal loads and strains, recovered using an inverse Fourier transform. Independently of the gust analysis, a 1g trim analysis is performed as per section (II.B). Using linear assumptions, the gust and 1g level flight responses are summed, so as to determine the total response as a function of time. Up- and down-gusts are considered by simply inverting the sign of the gust response. In order to reduce the amount of data for post-processing, the strain histories were only extracted at monitoring elements spread over the upper and lower skins, which allows the determination of the maximum strain time step. Subsequently, the strain for all elements at the critical time is calculated and, using the same approach as in section (II.B), a linear buckling analysis is also performed using the internal loads from the same time step. A small amount of structural damping (2%) is included in the gust analyses. It is important to note that for the frequency domain based gust analysis, it is assumed that the aeroelastic system from equation (4) is stable (i.e. no flutter or divergence has occurred).

E.   Control effectiveness analysis

The control effectiveness of the ailerons is an important consideration for the design of flexible wings because aileron loads tend to induce twisting of the wing, which reduces the spanwise aerodynamic incidence and, therefore, reduces the effective moment about the roll axis of the aircraft due to the aileron deflection. In extreme cases, control reversal may occur, where the roll moment due to the wing twist related aerodynamic forces exceeds that due to the aileron aerodynamic forces. For control effectiveness analyses, an aileron is placed on the doublet lattice mesh between 70% and 90% span and with a hinge line at 71% chord, as shown in Figure 1. In this study, the effectiveness $\Im$ of the aileron at inducing a roll maneuver is calculated as the ratio of the flexible wing to rigid wing steady roll rates $\dot{\phi}$ for the same aileron deflection β, such that

$$\Im = \frac{(\dot{\phi}/\beta)_{\text{flexible}}}{(\dot{\phi}/\beta)_{\text{rigid}}} \tag{9}$$

The system equation used to solve for the roll rate $\dot{\phi}$ is the same as equation (2) for the symmetric maneuver analysis, except that the extra aerodynamic points $\boldsymbol{u}_x$ now describe the input aileron deflection β, the unknown roll rate $\dot{\phi}$ and a steady roll maneuver with $\ddot{\phi} = 0$. An anti-symmetric load case is assumed, with the half-wing model only free to rotate about the roll axis, with all other degrees of freedom being constrained to zero at the wing root. The rigid fuselage and HTP are not included in this analysis, as they are not required for trimming.

III.   Optimization procedure of the wing-box

A.   Variables definition

The lower and upper wing skin properties are optimized independently in terms of thickness distributions $t_{L,U}(x,y)$ and composite laminate rotation angle distributions $\theta_{L,U}(x,y)$. The wing 1g shape is fixed, with 3mm thick aluminium spars and ribs and L-section aluminum stringers, as shown in Figure 1. The stringer attached flange is neglected and the other section dimensions vary linearly from $t_{str} = 13mm$, $h_{str} = 152mm$ at the wing root to $t_{str} = 4mm$ and $h_{str} = 51mm$ at the wing tip. The center wing-box (y ≤ 3m) is rigidly constrained, with fixed properties and it is not included in the wing structure mass calculation. The material properties are listed in Table 1. A symmetric and balanced homogenized laminate with constant 0/±45/90° ply percentages of [60/30/10] is used for both skins, with a minimum thickness of 3mm. A thick laminate with a large number of plies is assumed, so that variations in laminate thickness imply that several plies are dropped simultaneously to maintain the constant ply percentages within the laminate. The local laminate rotation angle is defined from the front spar direction to the local laminate's 0° ply fiber direction, such that for positive rotation angles the local 0° ply fibers run towards the leading edge of the wing, seen from the root to the tip of the wing. At any point on the skins, the ±45° and 90° ply fiber directions are defined relative to the local laminate's 0° ply fiber direction, and the laminate rotation angle varies between [-90°, 90°]. By rotating the orthotropic laminate and therefore the main fiber direction with respect to the wing span direction, shear-extension coupling is introduced in the wing skins, which results in bend-twist coupling at the wing level, due to the upper skin being in compression and the lower skin in tension under normal flight conditions.

In order to compare the performance of optimized straight-fiber and tow-steered laminates, four different composite laminate configurations are considered, based on the variation of the laminate rotation angle. The first two configurations use traditional straight fiber laminates; the first configuration constrains the laminate rotation angle to be zero on both the top and bottom skins ($\theta_{L,U} = 0$, 'UD' configuration) and the second allows the rotation angle on each skin to vary independently ($\theta_L = \theta_1$, $\theta_U = \theta_2$, 'UDrot' configuration). The third and fourth configurations assume tow-steered laminates, where the laminate rotation angle varies in the spanwise direction on both skins independently ($\theta_{L,U}(y)$, 'VAT' configuration) and where the laminate rotation angle varies in the spanwise and chordwise directions on both skins independently ($\theta_{L,U}(x,y)$, '2DVAT' configuration). The VAT configuration effectively assumes parallel tow paths for the 0° plies (although the ±45° and 90° ply tow paths may diverge and converge), whereas the 2DVAT configuration may also lead to diverging or converging tow paths for

the 0° plies. Approximate tow paths for the 0° plies are recovered using streamline functions, although additional work would be required to make the designs manufacturable in terms of defining actual tow paths with acceptable tow drops and overlaps [31]. As these features are not defined, the thickness distribution is assumed to be independent of the laminate rotation angle, and allowed to vary in the spanwise and chordwise directions on both skins independently. In the optimization results section (IV), figures show the approximate tow paths of the 0° plies only.

Thickness and rotation angle variables are defined at 44 control point locations distributed over each skin. Quadratic B-spline surfaces define smooth property variations between control points. B-splines were found to be a practical and reliable tool, as they guarantee that the properties between control points are bound by the control point values [32]. The control point locations on each skin are shown in Figure 2. The B-spline surfaces are defined in a rectangular space, which is mapped to the actual wing skin planform using the same B-spline interpolation. The knot vectors used are [0, 0, 0, 1/2, 1, 1, 1] in the chordwise direction and [0, 0, 0, [1/9:1/9:8/9], 1, 1, 1] in the spanwise direction. In the FEM model, each skin shell element has constant thickness and laminate properties, determined by projecting the location of the element centroid in the xy-plane onto the B-spline surface.
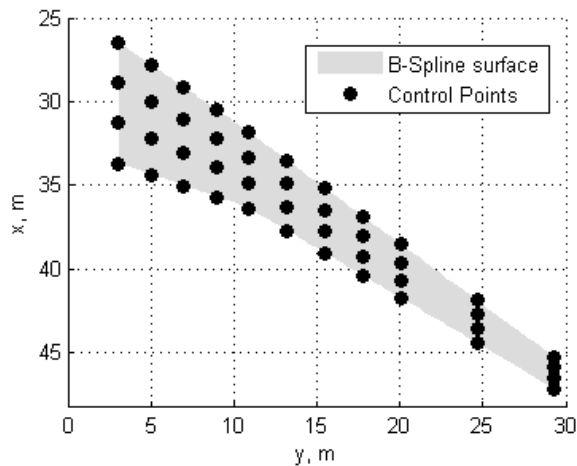

Figure 2 – Control point distribution on upper and lower skins

Table 1: Material Properties

Engineering constant	Unit	Value
Aluminum		
E	[GPa]	69
G	[GPa]	26
ν_{12}	–	0.32
ρ	$[10^3 \mathrm{kg/m^3}]$	2.7
Composite Ply		
E_{11}	[GPa]	128
E_{22}	[GPa]	11
ν_{12}	–	0.28
G_{12}	[GPa]	4.5
ρ	$[10^3 \mathrm{kg/m^3}]$	1.52

B. Optimization problem definition

Two types of optimizations were performed: the first type included constraints from only one type of analysis from sections (II.B) to (II.E), and the second type combined all constraints from all analyses. Both types of optimizations use objective functions that minimize the mass M_{wing} of the wing structure. The first type of optimization was mainly performed in order to gain a better understanding of the critical design features for different constraint types, whilst the second type of optimization led to the final conclusions in terms of comparing the performance of straight fiber and tow-steered laminates for aeroelastic tailoring. The first type of optimization was performed on the first three composite laminate configurations only, with spanwise thickness and laminate rotation angle variations only (UD, UDrot and VAT), reducing the number of variables and so facilitating interpretation of the results. The second type of optimization was performed on all four laminate configurations. The combined optimization problem constraints include buckling load factors λ_n, strains ε, damping factors ξ_h and control effectiveness $\Im$ values, calculated for eight different flight points listed in Table 2, which cover a range of different altitudes and Mach numbers. The aim is to compare the different optimal configurations for the chosen set of representative flight points, without these flight points corresponding necessarily the most critical design flight points. The symmetric maneuver and gust flight points have been arbitrarily chosen to be representative of a maximum cruise velocity flight point (FP1), of the design cruise flight conditions (FP2) and of a low altitude, low velocity flight point (FP3). The combined optimization problem may be stated as

$$\text{Min. } M_{wing}(t, \theta) \tag{10}$$

$$\text{s.t.} \quad \lambda_n(2.5\text{g, -1g , gusts}) \geq 1.7$$

$$\varepsilon(2.5\text{g, -1g , gusts}) \leq 3500\mu\varepsilon$$

$$\xi_h \geq 0$$

$$\Im \geq 50\%$$

The buckling and strain constraints only apply to the wing skins, because the spars and ribs were not modelled in sufficient detail to allow representative strain and buckling values to be calculated. Indeed, only one element was modelled through the height of the spars and ribs, such that no buckling there could have occurred. The buckling load constraint ensures that there is no buckling of the wing skins due to the applied trim and gust loads at limit load levels, where the empirical factor of 1.7 is used to approximate the buckling response of a more refined skin mesh as explained in section (II.B). The strain constraint of $3500\mu\varepsilon$ on the absolute value of the principal strains at limit load corresponds to an average strain damage tolerance constraint (such as used in reference [33]). The strain constraint was applied to all skin elements, and not just the monitoring elements mentioned previously (section II.D). To reduce the number of constraints, only the ten lowest buckling modes and the ten highest skin element strains were constrained for each load case and for each optimization iteration. More efficient failure-aggregation formulations, such as the KS-method [21] may be used in future work. It should be noted that, contrary to the buckling constraints, no empirical factor was applied to the maximum strains, because the accuracy of calculated peak strains depends more significantly on the amount of structural detail included in the model (such as 3D stringers, spar caps, manholes and fasteners), compared to the buckling modes, which are mainly driven by the overall panel stiffness, boundary conditions and mesh refinement. The inclusion of additional structural details would have resulted in significantly higher modelling and analysis costs and so was not pursued here. The strain constraint should therefore be viewed as an average or far-field strain constraint, rather than a local peak strain constraint.

The flutter constraint is implemented by calculating the damping factors ξ_h of the lowest ten flexible wing modes for each of the flutter flight points in Table 2, which are evenly spaced across the design flight altitudes, and then constraining these modes to be stable. Flight points 4 and 5 are representative of the conditions at 115% dive speed, which corresponds to the certification requirements, whereas the dynamic pressure for flight points 6, 7 and 8 was constrained by the available AIC data (limited to a maximum Mach number of 0.85). Finally, the control effectiveness constraint ensures that the optimized flexible wing design achieves at least 50% of the rigid wing

roll rate for a given aileron deflection at two different flight points. As the regulations do not specify a minimum acceptable control effectiveness value, an arbitrary value of 50% was chosen for this study. It should be noted that the control reversal speed is not explicitly calculated here. Moreover, other measures for the control effectiveness have been used in the literature [30], which have been shown to lead to lower roll rate ratios than 50%, and which would indicate that the constraint used here is rather conservative.

Importantly, that there is no constraint on the jig shape, which is implicitly calculated from the input 1g shape at each optimization iteration, as described in section (II.A).

Manufacturing constraints, such as constraints on the thickness gradient $\|\nabla t\|$ and fiber curvature $|k|$, could have been included in the optimization. However, initial studies indicated that the optimized solutions were unlikely to result in thickness gradients exceeding 1/8 (typical design value to limit the inter-laminar stresses in ply-drop regions [10]) or fiber radius of curvature below 0.5m (typical minimum radius for tow-steered laminates using automatic fiber placement methods [17]), due to the relatively wide spacing of the variable control points. Therefore, these constraints were not included in the optimization problem, but rather verified in a post-processing step on the optimized solutions. The thickness gradient $\|\nabla t\|$ was derived directly from the definition of the B-spline interpolation surface in terms of the thickness values at the control points and the 0° ply fiber curvature $|k|$ was estimated as $|k| = \|\nabla \times \theta_{L,U}(x,y)\|$ [22].

The gradient based optimization algorithm GCMMA [24] was chosen as the optimizer, since this has been successfully used in the past for tow-steered laminate optimizations, such as in reference [21]. Other optimization algorithms could have been investigated, such as the NASTRAN SOL200 internal gradient based optimizer, although it is not anticipated that this would have resulted in significant performance gains, as some constraint and gradient calculations would still have been performed outside NASTRAN. The objective function gradient and flutter and control effectiveness constraint function gradients were calculated in MSC NASTRAN SOL200. In this NASTRAN solution sequence, the direct method is used to solve for the grid deflection sensitivities, which are then used in a 'semi-analytical' formulation, making use of finite difference approximations, to derive the actual response sensitivities. The symmetric maneuver and gust constraints were calculated outside NASTRAN using forward finite differences, because there is currently no dynamic aeroelastic analysis capability in SOL200 and also because the evaluation of the buckling eigenvalues due to aeroelastic load cases was not possible in a single NASTRAN analysis run. For these external gradient calculations, additional NASTRAN trim, gust and buckling analyses were performed for each optimization variable using a fixed step size of 0.2mm thickness. It should be noted that the jig shape sensitivity was neglected for the gradient calculations. Weight convergence was

reached within 30 to 40 iterations. With one iteration taking up to 7hr (for 176 variables) on one 16 CPU node, which was mainly due to the NASTRAN external gradient calculations, relatively long optimization run times occurred. The current framework is therefore not appropriate for fast design assessments, unless faster gradient calculation methods can be implemented.

Table 2: Optimization Flight Points

Flight Point	Applicable Analyses	Altitude	Mach	Dynamic pressure (kPa)	Fuel Mass configurations
1	Symm. Maneuver; Control Effectiveness; Gusts	6.096 km (20000ft)	0.737	17.7	MZFW (MZFW and MTOW for gust analyses only)
2	Symm. Maneuver; Control Effectiveness; Gusts; Flutter	10.973 km (36000ft)	0.850	11.5	MZFW (MZFW and MTOW for gust and flutter analyses only)
3	Gusts	3.048 km (10000ft)	0.435	9.3	MZFW and MTOW
4	Flutter	0.000 km	0.649	29.9	MZFW and MTOW
5	Flutter	3.048 km (10000ft)	0.774	29.2	MZFW and MTOW
6	Flutter	6.096 km (20000ft)	0.850	23.6	MZFW and MTOW
7	Flutter	9.144 km (30000ft)	0.850	15.2	MZFW and MTOW
8	Flutter	12.192 km (40000ft)	0.850	9.5	MZFW and MTOW
Design	Jig Shape	10.973 km (36000ft)	0.850	11.5	(MZFW + MTOW)/2 (Fuel in outboard wing only)

IV.   Wing spanwise tailoring results and discussion

A.   Symmetric maneuver constraints only

The results for symmetric maneuvers are summarized in Table 3, which shows the design parameters for the different laminate configurations and indicates the critical constraints. For all 3 laminate configurations, the maximum strain constraint is active on the lower skin for the 2.5g pull-up load case and the buckling constraints become active on the lower and upper skins for the -1g and 2.5g cases respectively. Flight point 2 was found to be critical, because the aerodynamic lift moves outboard compared to flight point 1. Figure 3 shows the spanwise lift distributions for different cases and configurations. Both the VAT and UDrot configurations introduce additional wash-out on the outer wing through positive laminate rotation angles in high strain areas (Figure 4a),

particularly in the lower skin where the strain was not limited by 2.5g buckling constraints. The additional wash-out causes the center of lift of the wing to move inboard, reducing the loads applied to the outer wing and allowing the optimizer to further reduce the outboard skin thickness, with the lower skin thickness being reduced first (Figure 5a and 6a), so as to further increase the lower skin strain and the wash-out effect. For the VAT configuration, the thickness of the outer wing lower skin was mainly driven by the maximum strain constraint, with a large proportion of the lower skin reaching this constraint for the 2.5g case, as shown in Figure 7. For the UDrot and UD configurations, the lower skin thickness was also driven by the -1g buckling case, resulting in heavier configurations. Indeed, the VAT configuration not only reduced the outboard bending moment more so through increased wash-out, but the laminate rotation angle was closer to 45° in the outboard panels, which is known to increase the buckling load of rectangular panels [34].

The wash-out effect can be confirmed by plotting the local flexural axis of each configuration (Figure 8a), where the amount of wash-out is proportional to the forward movement of the flexural axis. The local flexural axis is defined as the locus of flexural centers along the wing, where the flexural center is the position of a shear load on a streamwise wing cross-section where there is zero twist on that cross-section relative to the wing root but not necessarily zero twist elsewhere on the wing [35]. The outer wing deflections and twist due to the maneuver loads for the UDrot and VAT configurations increase as shown in Figure 9.

Whilst positive laminate rotation angles are advantageous from a loads alleviation and buckling point of view in the outer wing, zero or slightly negative laminate rotation angles in the inner wing region allow loads to be redistributed, reducing stresses in buckling critical areas such as the rear-spar break and the area around the rear-spar/center wing-box joint. These areas are known to attract loads due to the geometry of aft-swept wings [36]. This pattern is clearly shown in Figure 4a for the VAT configuration and also explains the negative laminate rotation angle (-7deg) for the UDrot configuration in the upper skin. In conclusion, the VAT configuration achieves a greater wing structure mass reduction than the Udrot configuration (7.3% compared to 1.1%) by allowing different laminate rotation angles in the inner and outer wing skins, with similar optimum rotation angles in the upper and lower skins. The VAT configuration mass reduction is close to that found by Stanford [21] (6.1%) comparing maneuver optimized balanced straight-fiber and unbalanced spanwise tow-steered configurations, although that study also included laminate and chordwise thickness variations, which were not included here.

Table 3 also includes the more accurate buckling reserve factors calculated using the refined mesh, as described in section (II.B). It confirms that the current method results in conservative buckling load estimates, with the refined mesh buckling load factors all being larger than one. The coarse mesh buckling mode indicates localized

buckling occurs simultaneously over most of the planform, whereas the refined mesh buckles locally near the rear-spar/center wing-box joint only. This finding emphasizes the need for a different approach if the buckling eigenvalues and modes are to be calculated accurately, possibly at the expense of a greater computational time.

Table 3: Wing spanwise tailoring results with symmetric maneuver constraints only (active constraints in bold font)

| Configuration [number of variables]	UD [22]	UDrot [24]	VAT [44]
Wing Structure Mass (kg)	10579	10466	9812
Wing Structure Mass reduction (%)	(baseline)	1.1	7.3
Critical Flight Point (from Table 2)	FP2	FP2	FP2
2.5g Buckling Reserve Factor $\lambda_n(2.5g)$ [Refined mesh Buckling Reserve Factor]	**1.70** [1.38]	**1.70** [1.38]	**1.70** [1.45]
-1g Buckling Reserve Factor $\lambda_n(-1g)$ [Refined mesh Buckling Reserve Factor]	**1.70** [1.19]	**1.70** [1.18]	**1.70** [1.19]
2.5g Maximum Absolute Principal Strain, $\varepsilon(2.5g)$ (με)	**3.5E3**	**3.5E3**	**3.5E3**
-1g Maximum Absolute Principal Strain, $\varepsilon(-1g)$ (με)	1.7E3	1.6E3	1.5E3
Design FP Root Angle of Attack (deg)	2.1	2.1	2.2
FP2(2.5g, -1g) Root Angle of Attack (deg)	6.7, -5.1	7.0, -5.4	7.1, -5.6
Maximum Absolute thickness gradient, $\|\nabla t\|$ (m/m)	0.006	0.008	0.004
Smallest Radius of Curvature for the 0° fibers, $|k|^{-1}$ (m)	N/A	N/A	4.9
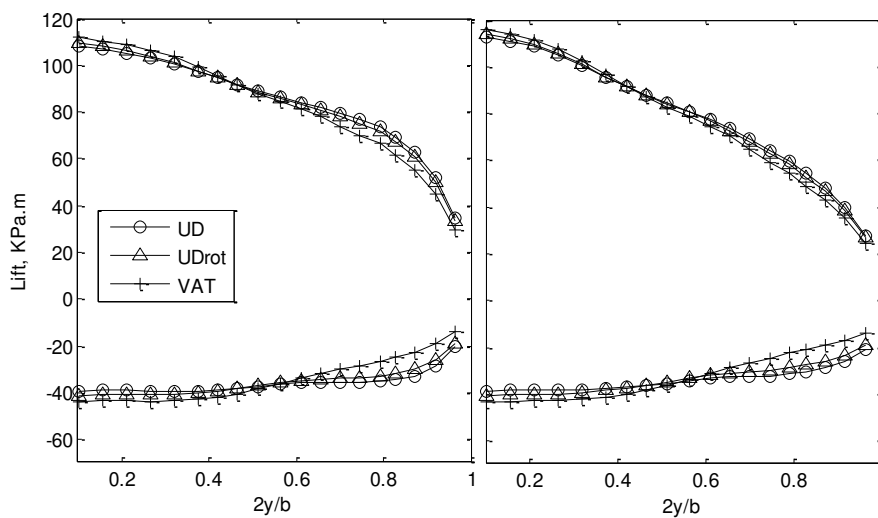
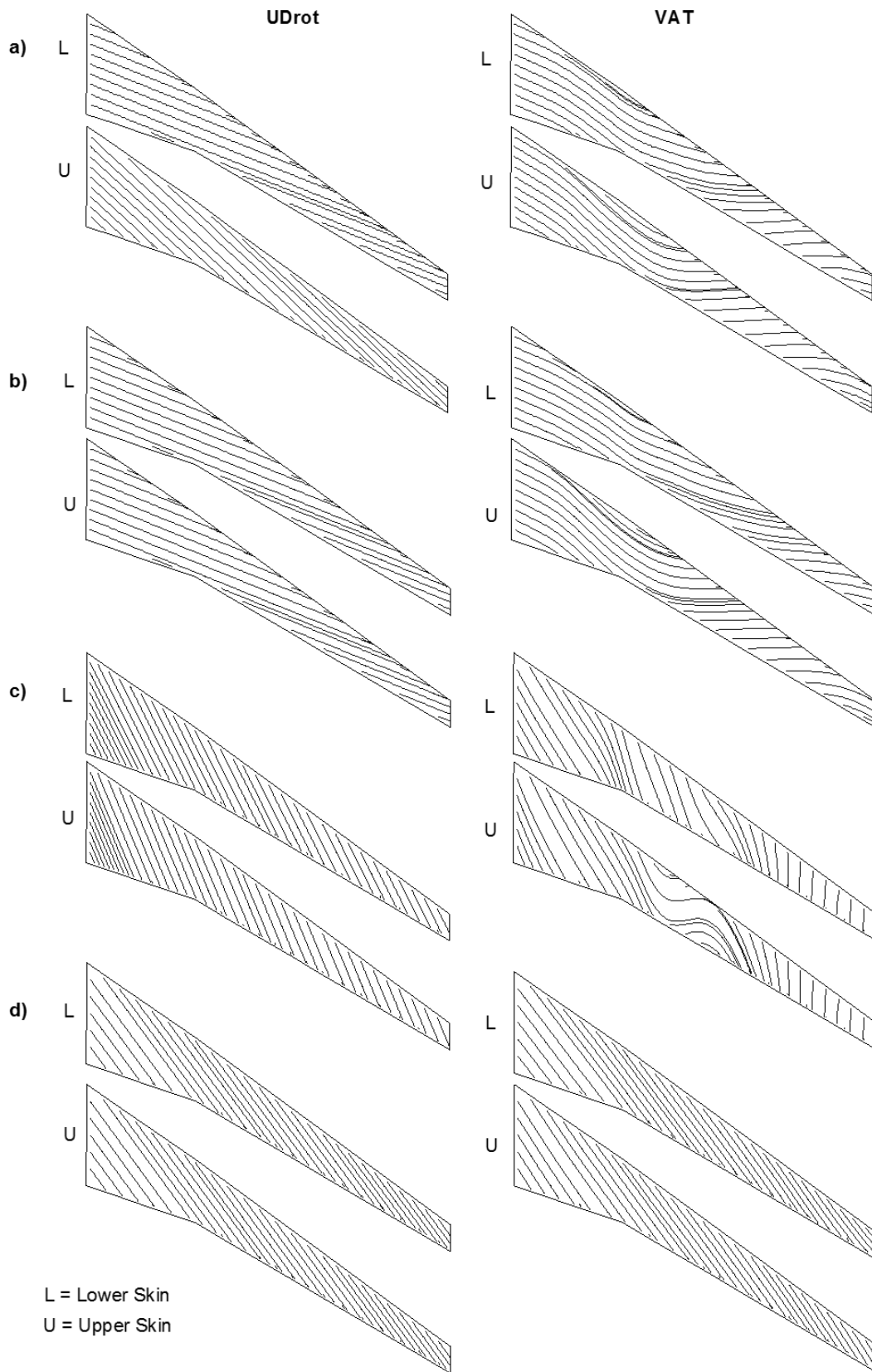Figure 3: Trimmed 2.5g and -1g lift distributions at MZFW for FP1 (right) and FP2 (left)

Figure 4: Tow paths for the 0° plies on the UDrot and VAT configurations, for a 1D optimization with a) symmetric maneuver constraints, b) gust constraints, c) flutter constraints, d) control effectiveness constraints only
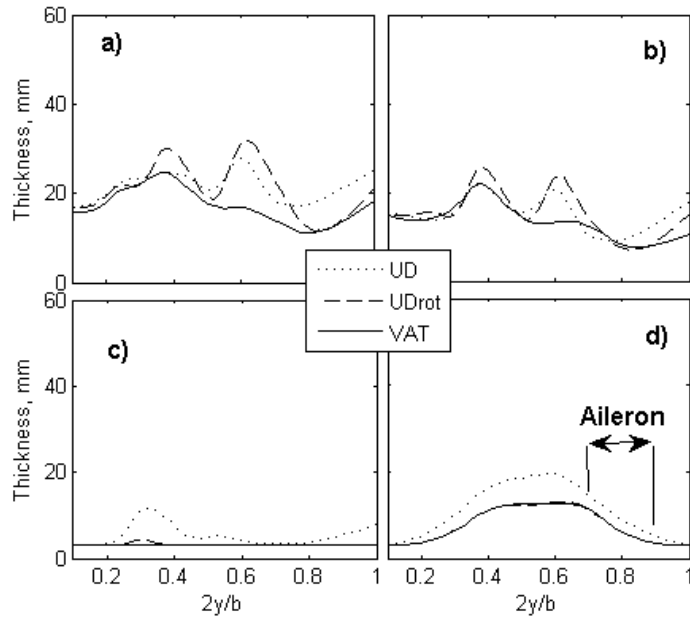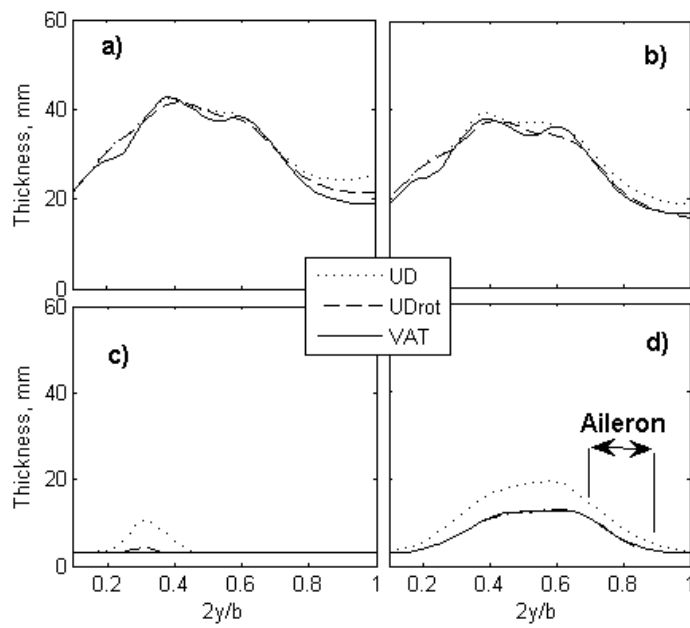
Figure 5: Spanwise Thickness distributions on lower skins, for a 1D optimization with a) symmetric maneuver constraints, b) gust constraints, c) flutter constraints, d) control effectiveness constraints only

Figure 6: Spanwise Thickness distributions on upper skins, for a 1D optimization with a) symmetric maneuver constraints, b) gust constraints, c) flutter constraints, d) control effectiveness constraints only
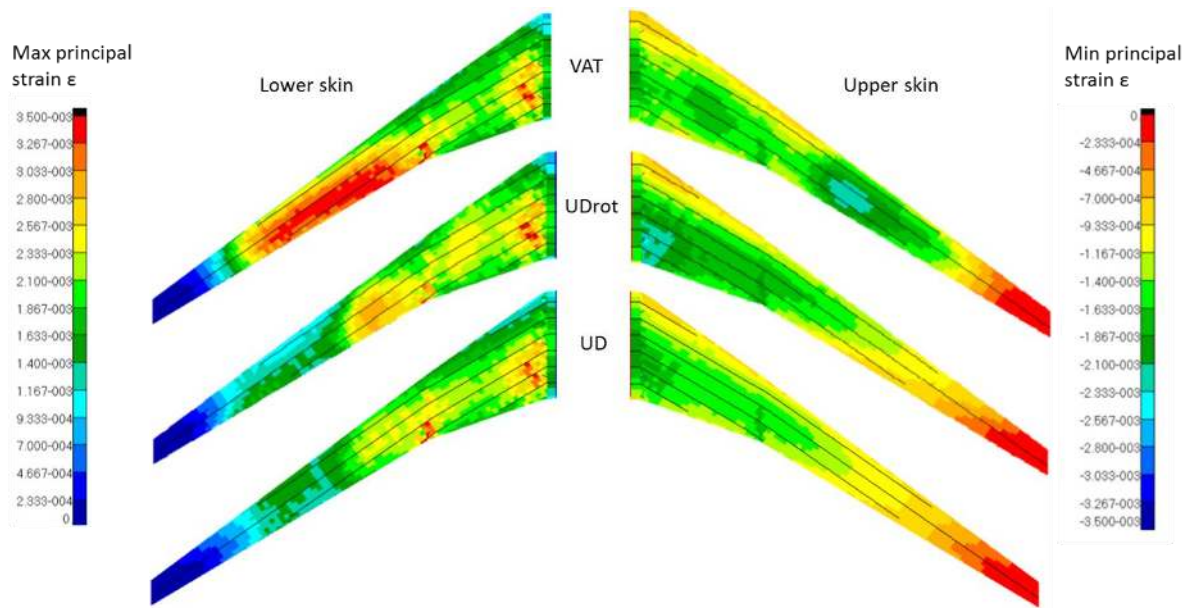
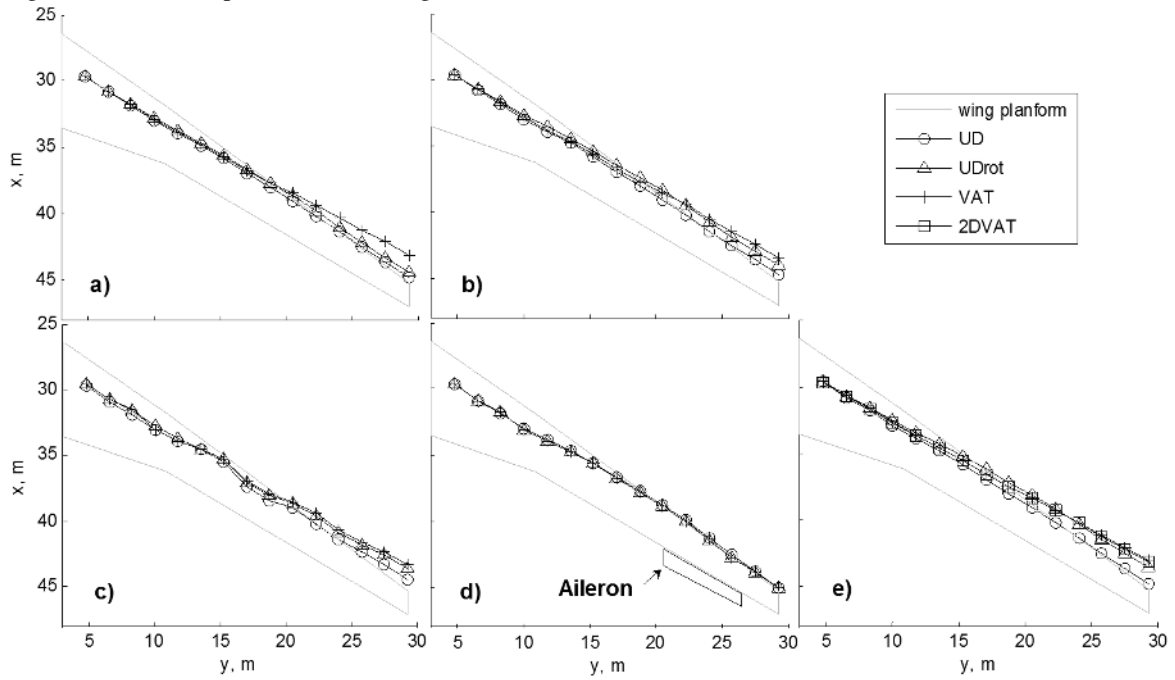Figure 7: Strain comparison for the 2.5g load case

Figure 8: Local flexural axes relative to wing structure planform, for a 1D optimization with a) symmetric maneuver constraints, b) gust constraints, c) flutter constraints, d) control effectiveness constraints only and e) for a 2D optimization with all combined constraints
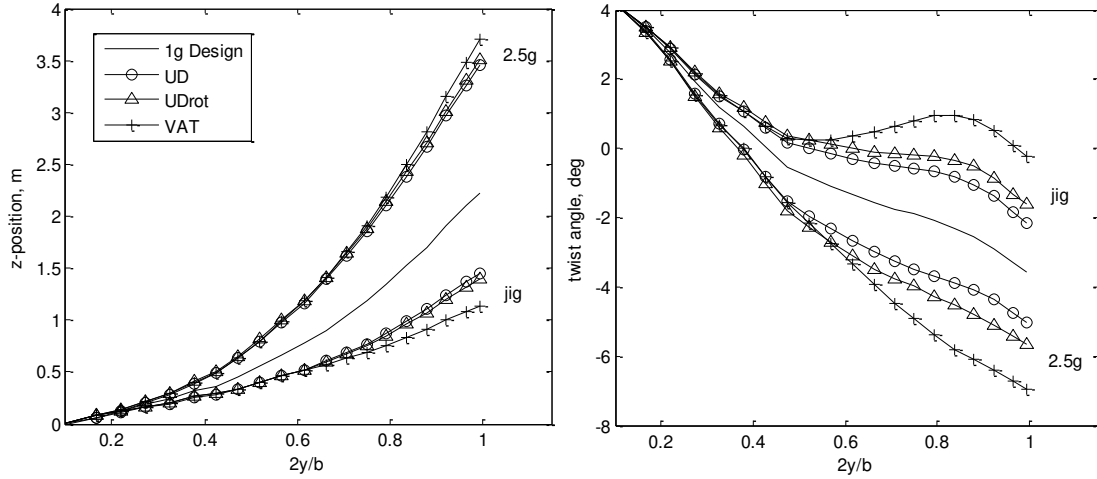
Figure 9: Z-position and twist along the span for the 1g design shape, the jig shapes and at 2.5g shapes

B.   Gust constraints only

Table 4: Wing spanwise tailoring results with gust constraints only (active constraints in bold font)

Configuration [number of variables]	UD [22]	UDrot [24]	VAT [44]
Wing Structure Mass (kg)	9182	9091	8724
Wing Structure Mass reduction (%)	(baseline)	1.0	5.0
Critical Flight Point (from Table 2)	FP2 (MTOW)	FP2 (MTOW)	FP2 (MTOW)
Gust Buckling Reserve Factor λ_n(gust)	**1.70**	**1.70**	**1.70**
Gust Maximum Absolute Principal Strain, ε(gust) (με)	**3.5E3**	**3.5E3**	**3.5E3**
Design FP Root Angle of Attack (deg)	2.1	2.2	2.2
Critical gust gradient, H (m)	96m	85m	85m
Maximum Absolute thickness gradient, $\|\nabla t\|$ (m/m)	0.006	0.008	0.004
Smallest Radius of Curvature for the 0° fibers, $|k|^{-1}$ (m)	N/A	N/A	6.01

The gust results are summarized in Table 4, where all configurations are shown to be aeroelastically stable. FP2 with a MTOW mass configuration was found to be the critical flight point for all configurations. The mass reductions for the UDrot and VAT configurations are similar to those achieved for the symmetric maneuver optimization in section (IV.A). The VAT and UDrot configurations once again generate additional wash-out through positive laminate rotation angles in high strain areas on the outer wing (Figure 4b), with the largest thickness reductions observed in the outboard lower skin (Figure 5b and 6b).

The critical strain histories are compared in Figure 10. The strain level at t=0s, corresponds to the steady 1g trim strain, which contributes approximately 60% of the peak strain with the rest due to the gust response. In all cases, the peak strain occurs at the first up-bend deflection of the wing (swing-back) due to a down-gust. The response

frequency closely matches the first bending mode of the wing at that flight point (1.7Hz) and the peak strains occur in similar locations on the skins as for the symmetric maneuver case, which indicates that the first bending mode is the main mode excited by the gust. The longer gust wavelengths (H=85-96m), with higher gust velocities, generate higher strain levels as shown in Figure 11. This figure also shows that the VAT configuration has mostly higher strains for all gust lengths than the UDrot configuration, which, in turn, has mostly higher strains than the UD configuration.

The UDrot configuration has a positive rotation angle in the upper skin, which is different from the symmetric maneuver solution from section (IV.A). Due to the lower wing root bending moment (MX) and torque (MY), as shown in Figure 12, less load redistribution inboard is traded for more wash-out outboard. The resulting local flexural axes are plotted in Figure 8b and it can be seen how the VAT solution again moves the flexural axis forward (but not as much as for the maneuver case), which increases the amount of wash-out generated from a vertical gust.
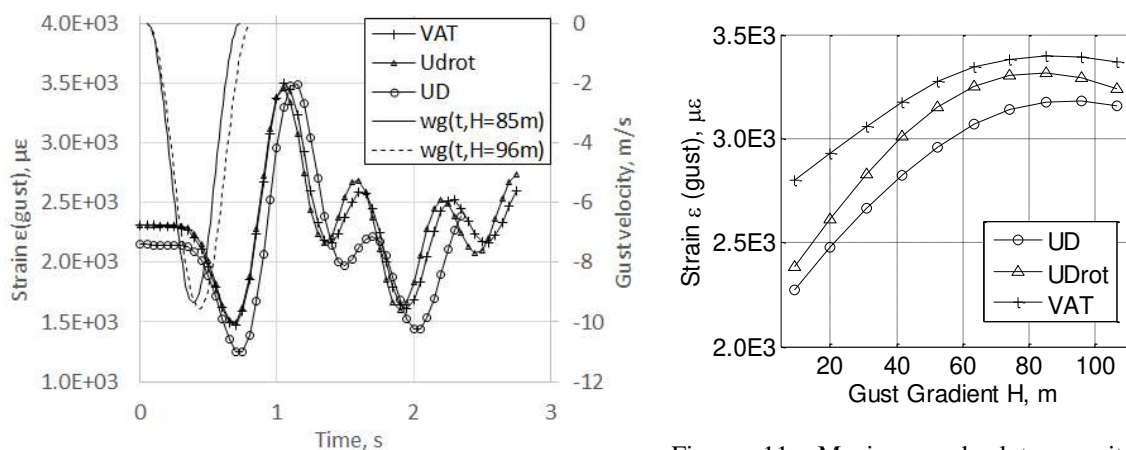

Figure 10: Critical Strain histories

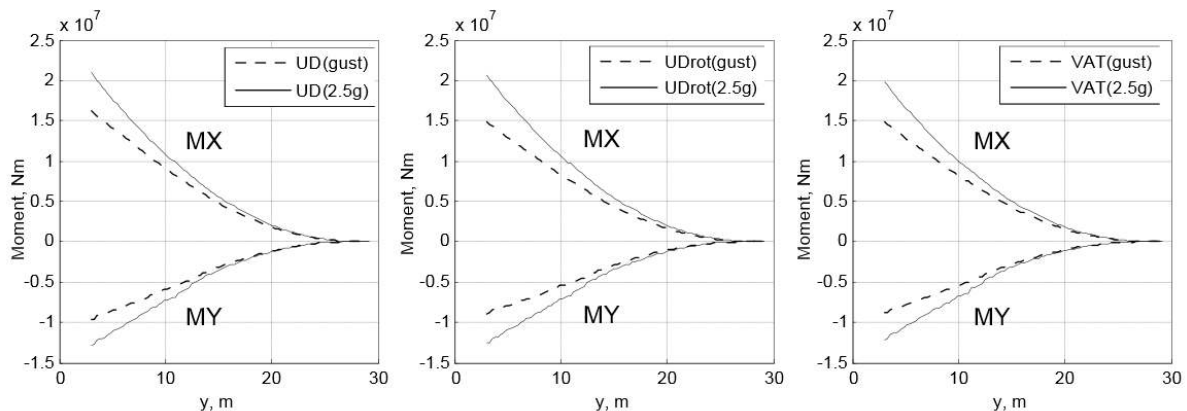Figure 11: Maximum absolute monitoring element strain as a function of gust length

Figure 12: Bending moment and Torque distribution for the 2.5g symmetric maneuver and critical gust load cases

C. Flutter constraints only

The flutter results are summarized in Table 5. The thickness plots in Figures 5c and 6c, show that the optimizations resulted in excessively low mass wing structures because no strain or buckling constraints were enforced. The lowest mass was reached for the VAT configuration, where all skin thicknesses were reduced to the minimum value of 3mm. Both the VAT and the UDrot configurations achieve significantly lighter wing structures compared to the UD configuration, by using negative laminate rotation angles in both skins. However, the negative laminate rotation angle did not result in increased wash-in, as can be seen in the flexural axis plots (Figure 8c). On the contrary, the UDrot and VAT configurations, being more flexible, still generate more wash-out than the UD configuration. Indeed, whilst the laminate rotation angle is close to -31° in the UDrot configuration, which is the rotation angle for maximum shear-extension coupling (A_{16}), the laminate driven wash-in effect was found to be negligible compared to the sweep driven wash-out effect, which is amplified due to the reduced bending stiffness (A_{11}) of the wing at laminate rotation angles of 30° or more. It is important to emphasize that these laminate stiffness properties A_{16} and A_{11} are the effective properties measured in the main load application direction along the wing span, and not the properties measured in the main laminate material directions (which are of course fixed, with $A_{16}=0$).

The laminate angle was also optimized to yield vibration mode shapes and frequencies that increase the flutter velocity. To illustrate this effect, the flexible mode vibration frequencies and damping ratios are plotted against Mach number (at constant altitude=0km, equivalent to FP4) in Figure 13. The UD configuration experiences a 'soft' flutter at M=0.64 due to an interaction of the first bending and torsion modes, with the mode 2 (2.7Hz) damping briefly becoming negative. The frequencies and mode shapes of the UDrot and VAT configuration are modified so as to avoid this flutter mode, with flutter occurring at M=0.69 and 0.66 respectively at FP4 due to the interaction of higher frequency modes, such that the flutter constraint is inactive at FP4 for these configurations. The UDrot and VAT configurations are instead driven by the flutter constraint at FP6, which becomes active for both configurations.

It should be noted that the flight points FP 6, 7 and 8 used for this study were constrained by the available transonic AIC data, which was limited to a maximum Mach number of 0.85. In reality, the configurations would have to be shown to be flutter free up to the dive velocity+15%. Had a higher Mach number flutter boundary been considered at higher altitudes, it is possible that the optimal skin thickness distributions and laminate rotations angles would have changed for all configurations. For the UDrot and VAT configurations, a change in laminate rotation angles would have affected the mode shapes and vibration frequencies, potentially increasing the flutter speed without

necessarily implying significant wing weight increases. This behavior has been found in previous work, using a constant thickness unswept wing model [20].

Table 5: Wing spanwise tailoring results with flutter constraints only (active constraints in bold font)

| Configuration [number of variables]	UD [22]	UDrot [24]	VAT [44]
Wing Structure Mass (kg)	3689	3131	3081
Wing Structure Mass reduction (%)	(baseline)	15.1	16.5
Critical Flight Point (from Table 2)	FP4 (MZFW)	FP6 (MTOW)	FP6 (MTOW)
Flutter Damping Coefficient, ξ_h (%)	**0.0**	**0.0**	**0.0**
Critical Mass Configuration	MZFW	MTOW	MTOW
Critical Altitude and Mach number	0km, M=0.649	6096 km, M=0.85	6096 km, M=0.85
Maximum Absolute thickness gradient, $\|\nabla t\|$ (m/m)	0.004	0.001	0.000
Smallest Radius of Curvature for the 0° fibers, $\|k\|^{-1}$(m)	N/A	N/A	1.47
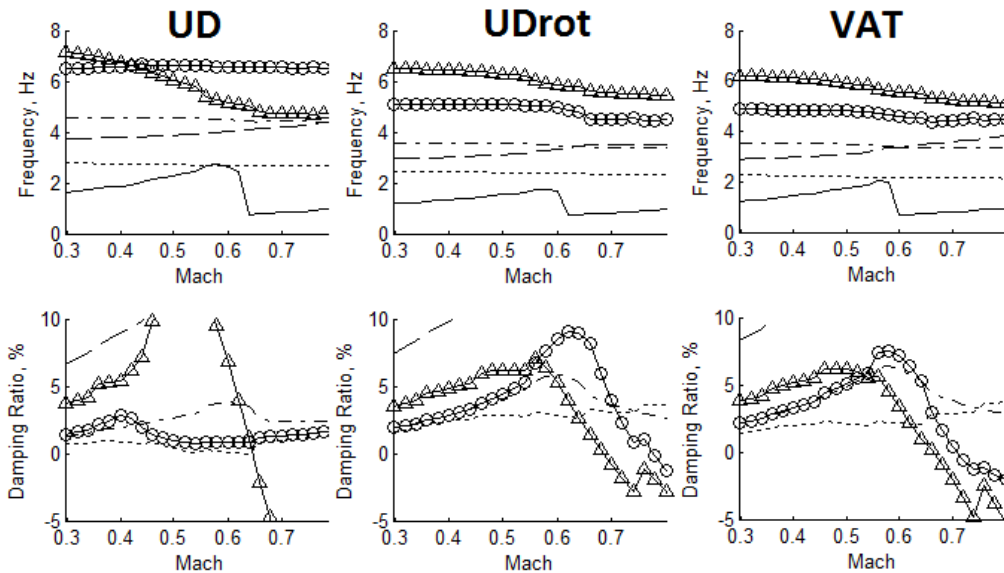
Figure 13: Frequency and damping as a function of Mach number at sea-level (FP4) for the first 6 flexible modes (all configurations at MZFW)

D.   Control effectiveness constraints only

The control effectiveness results are summarized in Table 6. As no buckling or strain constraints were implemented, excessively low mass configurations are achieved, where all three configurations have active control effectiveness constraints at FP1. The same mass reduction was found for both the VAT and UDrot configurations, with almost identical thickness and laminate rotation angle distributions in both configurations (Figures 4d, 5d, 6d). A constant laminate rotation angle of approximately -18° generates additional wash-in in the outer wing and allows a more flexible wing for the same amount of control effectiveness. Indeed, the flexural axis locations are identical for all three configurations (Figure 8d), indicating that the negative wing twist due to the

aileron deflection is the same for all configurations. This result was verified by plotting the lift distribution for the UD and VAT configurations in Figure 14 and, as expected, the lift distributions for the flexible wings are the same. The optimized thickness and laminate rotation angle distributions did not show any local features near the aileron location, indicating that the optimum solutions are driven by the overall wing behavior.

It may be noted that the configurations generate more wash-in than the flutter constraint optimized configurations from section (IV.C) because the bending stiffness is reduced less for a laminate rotation angle of -18° than for one of -31°, reducing the wash-out due to the wing sweep.

Table 6: Wing spanwise tailoring results with control effectiveness constraints only (active constraints in bold font)

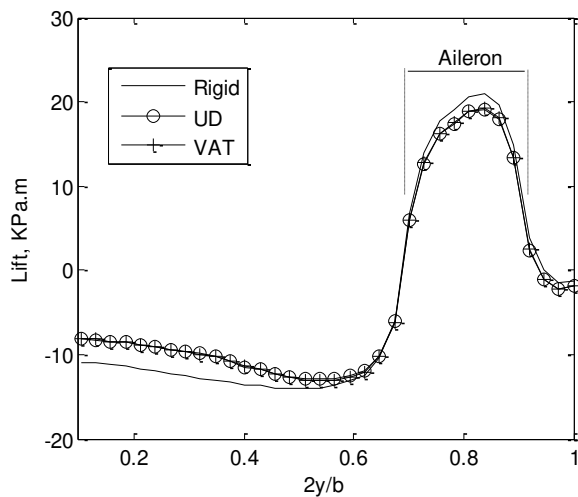| Configuration [number of variables]	UD [22]	UDrot [24]	VAT [44]
Wing Structure Mass (kg)	5562	4496	4496
Wing Structure Mass reduction (%)	(baseline)	19.2	19.2
Critical Flight Point (from Table 2)	FP1	FP1	FP1
Control Effectiveness, $\Im$ (%)	**50**	**50**	**50**
Maximum Absolute thickness gradient, $\|\nabla t\|$ (m/m)	0.003	0.002	0.002
Smallest Radius of Curvature for the 0° fibers, $|k|^{-1}$ (m)	N/A	N/A	71.61

Figure 14: Roll trimmed flexible and rigid wing lift distributions (FP1), for zero acceleration and 15° aileron deflection

E.   Optimization with all combined constraints

The combined constraint optimizations used initial values obtained from the optimized symmetric maneuver configurations identified in section (IV.A). No changes in thickness, laminate rotation angles or wing mass were

found, as only the trimmed maneuver strain and buckling constraints remain active. The gust, flutter and control effectiveness constraint values found for the trim configurations are summarized in Table 7. By starting the optimizations at different points, similar solutions were found, with wing mass reductions of 2%, 4% and 2% for the UD, UDrot and VAT solutions respectively compared to the first set of optimizations. The main difference was that the second optimized UDrot configuration had positive rotation angles on both upper and lower skins, which resulted in more wash-out on the outer wing and allowed the outboard lower skin thickness to be reduced compared to the previous UDrot solution. However, the forward fiber sweep on the top skin increased loads around the rear spar kink on the top skin, causing the top skin thickness to increase around this area compared to the previous solution. This thickness trade-off lead to only 4% mass reduction compared to the first UDrot optimization.

There are several possible reasons for the designs to be uniquely driven by the symmetric maneuver constraints. It may be that some gust or flutter critical flight points are not considered, or that the constraint formulations are overly simplified. It is worth noticing that the gust constraints are not far from being active (e.g. <10% margin for the VAT configuration) and that a different choice of flight cases could have resulted in gust critical designs here. It is also interesting to note that the control effectiveness seems to reduce as the design freedom is increased, from 20% margin for the UD configuration to only 2% margin for the VAT configuration. Indeed, as the wash-out coupling increases, the control effectiveness reduces because the moment arm between the flexural axis and the aileron increases.

Table 7: Wing spanwise (1D) tailoring results with combined constraints

Configuration [number of variables]	UD [22]	UDrot [24]	VAT [44]
Wing Structure Mass (kg)	10579	10466	9812
Wing Structure Mass reduction (%)	(baseline)	1.1	7.3
Critical Flight Point (from Table 2)	FP2	FP2	FP2
Active Constraints	λ_n(2.5g, -1g) = 1.70 ε(2.5g) = $3.5E3\mu\varepsilon$	λ_n(2.5g, -1g) = 1.70 ε(2.5g) = $3.5E3\mu\varepsilon$	λ_n(2.5g, -1g) = 1.70 ε(2.5g) = $3.5E3\mu\varepsilon$
Inactive Constraints	ε(-1g) = $1.7E3\mu\varepsilon$ λ_n(gust) = 1.86 ε(gust) = $2.9E3\mu\varepsilon$ ξ_h = 0.1% $\Im$ = 70%	ε(-1g) = $1.6E3\mu\varepsilon$ λ_n(gust) = 2.11 ε(gust) = $2.6E3\mu\varepsilon$ ξ_h = 0.1% $\Im$ = 65%	ε(-1g) = $1.5E3\mu\varepsilon$ λ_n(gust) = 1.86 ε(gust) = $3.2E3\mu\varepsilon$ ξ_h = 0.1% $\Im$ = 52%

V.   Wing spanwise and chordwise tailoring (2D) results and discussion

The combined constraint optimizations were repeated allowing a spanwise and chordwise variation of the thickness (UD, UDrot and VAT configurations) and also of the laminate rotation angle (for the 2DVAT configuration only). The results are summarized in Table 8, with Figures 15, 16 and 8e showing the optimized laminate rotation angle distributions, the skin thickness distributions and the local flexural axis locations. As expected, by increasing the number of variables, the wing mass is reduced compared to the equivalent configurations from section (IV.E), with a maximum mass reduction of 12% for the 2DVAT configuration compared to the UD configuration with spanwise thickness variation only.

Interestingly, the UDrot configuration with spanwise and chordwise thickness variation achieves a similar wing mass to the VAT configuration with only spanwise thickness variation. Looking at the thickness and flexural axis plots in Figures 16 and 8e, the UDrot configuration achieves a larger amount of wash-out in the outer wing by reducing the lower skin thickness towards the rear spar around 2y/b=0.6, while keeping a thicker skin section towards the front spar. The higher strain levels towards the rear spar and the shifting of the shear center of the wing-box section forward not only increase the wash-out, but also redistribute the loads towards the front spar, which ensures that the now thinner panels towards the rear spar carry less load and do not buckle prematurely.

The 2DVAT configuration also achieves a wing structure mass reduction of over 300kg compared to the VAT configuration. This result was mainly due to a chordwise laminate rotation angle change in the upper skin inboard of the rear spar break, which can be seen in Figure 15, where the zero degree fibers align with the front spar towards the leading edge and rotate by a negative angle towards the trailing edge. This effect stiffens the leading edge and allows the thickness there to reduce, whilst maintaining the same load alleviation in the rear-spar break area as for the VAT configuration. Similar laminate rotation angle distributions and mass reductions factors were recently found by Brooks et al [22] for a higher aspect-ratio wing derived from the NASA CRM model, although that study included additional structural and wing shape variables that are not considered here.

The control effectiveness constraint is active for the 2DVAT configuration and, just as in the previous section, the control effectiveness reduces as the design freedom is increased and as the wash-out increases for load and weight reduction.

Table 8: Wing spanwise and chordwise (2D) tailoring results with combined constraints

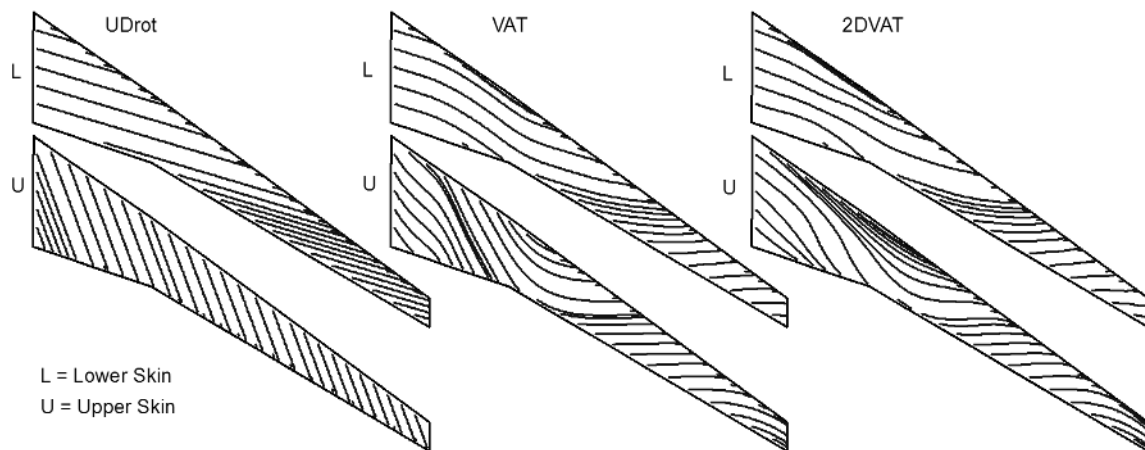| Configuration [number of variables]	UD [88]	UDrot [90]	VAT [110]	2DVAT [176]
Wing Structure Mass (kg)	10352	9835	9581	9268
Wing Structure Mass reduction (%)	(baseline)	5.0	7.4	10.5
Critical Flight Points (from Table 2)	FP2	FP2	FP2	FP1, FP2
Active Constraints	λ_n(2.5g, -1g) = 1.70 ε(2.5g) = 3.5E3με	λ_n(2.5g, -1g) = 1.70 ε(2.5g) = 3.5E3με	λ_n(2.5g, -1g) = 1.70 ε(2.5g) = 3.5E3με	λ_n(2.5g, -1g) = 1.70 @ FP2 ε (2.5g) = 3.5E3 μ ε @ FP2 $\Im$ = 50% @ FP1
Inactive Constraints	ε(-1g) = 1.7E3με λ_n(gust) = 1.86 ε(gust) = 2.9E3με ξ_h = 0.1% $\Im$ = 69%	ε(-1g) = 1.6E3με λ_n(gust) = 1.86 ε(gust) = 3.2E3με ξ_h = 0.1% $\Im$ = 57%	ε(-1g) = 1.6E3με λ_n(gust) = 1.85 ε(gust) = 3.2E3με ξ_h = 0.1% $\Im$ = 51%	ε(-1g) = 1.4E3με λ_n(gust) = 1.87 ε(gust) = 3.2E3με ξ_h = 0.1%
Maximum Absolute thickness gradient, $\|\nabla t\|$ (m/m)	0.018	0.016	0.006	0.022
Smallest Radius of Curvature for the 0° fibers, $\|k\|^{-1}$ (m)	N/A	N/A	5.23	2.03

Figure 15: Tow paths for the 0° plies on the Udrot, VAT and 2DVAT configurations, for a 2D optimization with all combined constraints
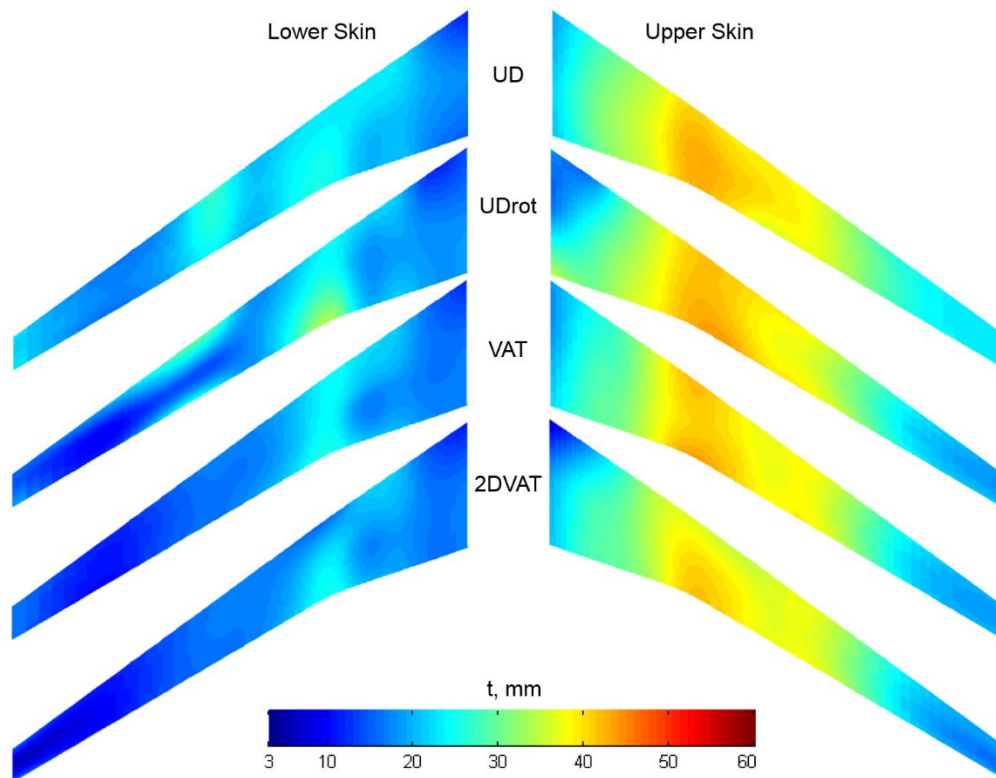
Figure 16: Thickness distributions on upper and lower skins, for a 2D optimization with all combined constraints

VI.   Conclusions

A realistic wing-box model has been aeroelastically tailored using straight fiber and tow-steered laminates in the upper and lower wing skins. The variables include the local laminate thickness and rotation angle, for a locally homogenized, orthotropic, constant-ply-percentage laminate. The 3D structural model, representative of the NASA Common Research Model aft-swept wing, is coupled to the doublet lattice aerodynamic model that is implemented within MSC NASTRAN, so allowing the wing loads and deflections to update with changes in stiffness. A gradient based optimizer was used to minimize the wing mass, with constraints on the 1g flight shape, on the strains and buckling loads due to steady 2.5g/-1g maneuver and dynamic gust loads, and with constraints on the flutter stability and control effectiveness for a number of different flight conditions. Initially, the wing was optimized for each constraint separately to identify which design features were driven by the different constraints. Then, the wing was optimized for all combined constraints, first only considering spanwise (1D) variable distributions and then also spanwise and chordwise (2D) variable distributions.

It was found that the thickness and laminate rotation angles in the upper skin were mainly driven by the 2.5g maneuver buckling constraints, whilst the lower skin properties were mainly driven by the 2.5g strain and the -1g buckling constraints. Optimizing the wing only for discrete up/down gust load cases resulted in similar, although

somewhat lighter wing structures, as the wing root bending moment due to the gusts is less than that from maneuver loads. For the combined constraint optimizations, the gust constraints were found to be nearly active in some cases, indicating that a slightly different choice of flight cases could result in the gust loads driving the skin properties in the outer wing.

To reduce the effects of maneuver and gust loads, the optimum configurations rotated the main fiber direction forward of the front spar direction in the outer wing, so as to induce a wash-out effect, which was particularly effective as the outer wing flexibility increased. In the inner wing, the optimal main fiber direction was rotated aft of the front spar, so as to redistribute the loads from the rear spar into the front spar, which alleviates high strain areas around the rear spar.

As expected, the tow-steered configurations achieve the largest mass reductions (7.3% and 10.5% for the 1D and 2D optimizations respectively) compared to the straight-fiber configuration where the main fiber direction aligns with the front spar direction. For the 2D optimizations, a 5% mass reduction was also achieved by allowing a rotation of the straight fiber laminate main fiber direction in each skin independently and by allowing a chordwise thickness variation, where the laminate rotations in each skin were dictated by a compromise between increasing the wash-out in the outer wing and increasing the load redistribution in the inner wing.

The control effectiveness was found to reduce as the design freedom increased, and as the wash-out for load and weight reduction increased. This implies that if a higher level of control effectiveness had been required (e.g. 60%), the weight savings associated with tow-steering would have been reduced. It should also be highlighted that the maximum ply drop rate (0.022) and minimum fiber radius of curvature (2.03m) found for the combined constraint optimizations are well within the current manufacturing capabilities using automatic fiber placement (AFP) technology.

The presented optimization framework could be extended to a larger number of variables and constraints, by increasing the number of control points, by including spar and stringer thicknesses as variables, by allowing laminate ply percentages to change or by considering additional flight-points, for example. Multi-scale/multi-fidelity approaches for calculating accurate constraint values (such as buckling loads) could also be included in the analysis. The framework may, in the future, be adapted to investigate the aeroelastic tailoring of very flexible, geometrically nonlinear wings.

VIII.   References

[1] J.R. Wright and J.E. Cooper, *Introduction to Aircraft Aeroelasticity and Loads*. 2007, Wiley, pp.xix-xxiv

[2] N. Krone, J. R., *Divergence elimination with advanced composites*, in *Aircraft Systems and Technology Meeting*. 1975, American Institute of Aeronautics and Astronautics.
doi: 10.2514/6.1975-1009

[3] M.H. Shirk, T.J. Hertz, and T.A. Weisshaar, *Aeroelastic tailoring - Theory, practice, and promise.* Journal of Aircraft, 1986. **23**(1): pp. 6-18.
doi: 10.2514/3.45260

[4] F.E. Eastep, V.A. Tischler, V.B. Venkayya, and N.S. Khot, *Aeroelastic Tailoring of Composite Structures.* Journal of Aircraft, 1999. **36**(6): pp. 1041-1047.
doi: 10.2514/2.2546

[5] T.A. Weisshaar and D.K. Duke, *Induced Drag Reduction Using Aeroelastic Tailoring with Adaptive Control Surfaces.* Journal of Aircraft, 2006. **43**(1): pp. 157-164.
doi: 10.2514/1.12040

[6] C.L. Pettit and R.V. Grandhi, *Optimization of a Wing Structure for Gust Response and Aileron Effectiveness.* Journal of Aircraft, 2003. **40**(6): pp. 1185-1191.
doi: 10.2514/2.7208

[7] T.U. Kim and I.H. Hwang, *Optimal design of composite wing subjected to gust loads.* Computers & Structures, 2005. **83**(19-20): pp. 1546-1554.
doi: 10.1016/j.compstruc.2005.02.002

[8] H. Arizono and K. Isogai, *Application of Genetic Algorithm for Aeroelastic Tailoring of a Cranked-Arrow Wing.* Journal of Aircraft, 2005. **42**(2): pp. 493-499.
doi: 10.2514/1.392

[9] J. K. S. Dillinger, T. Klimmek, M. M. Abdalla, and Z. Gürdal, *Stiffness Optimization of Composite Wings with Aeroelastic Constraints*, Journal of Aircraft, 2013. **50**(4): pp. 1159-1168.
doi: 10.2514/1.C032084

[10] A. Mukherjee and B. Varughese, *Design guidelines for ply drop-off in laminated composite structures.* Composites Part B-Engineering, 2001. **32**(2): pp. 153-164.
doi: 10.1016/S1359-8368(00)00038-X

[11] C.S. Lopes, Z. Gurdal, and P.PP. Camanho, *Variable-stiffness composite panels: Buckling and first-ply failure improvements over straight-fiber laminates.* Computers & Structures, 2008. **86**(9): pp. 897–907
doi: 10.1016/j.compstruc.2007.04.016

[12] Z. Gurdal, B.F. Tatting, and C.K. Wu, *Variable stiffness composite panels: Effects of stiffness variation on the in-plane and buckling response.* Composites Part a-Applied Science and Manufacturing, 2008. **39**(5): pp. 911–922
doi: 10.1016/j.compositesa.2007.11.015

[13] S.-Y. Kuo and L.-C. Shiau, *Buckling and vibration of composite laminated plates with variable fiber spacing.* Composite Structures, 2009. **90**(2): pp. 196-200
doi: 10.1016/j.compstruct.2009.02.013

[14] Z. Wu, P.M. Weaver, G. Raju, and B. Chul Kim, *Buckling analysis and optimization of variable angle tow composite plates.* Thin-Walled Structures, 2012. **60**(1): pp. 163-172.
doi: 10.1016/j.tws.2012.07.008

[15] C.S. Lopes, Z. Gurdal, and P.P. Camanho, *Tailoring for strength of composite steered-fiber panels with cutouts.* Composites Part a-Applied Science and Manufacturing, 2010. **41**(12): pp. 1760–1767
doi: 10.1016/j.compositesa.2010.08.011

[16] K. Gliesche, T. Hubner, and H. Orawetz, *Application of the tailored fiber placement (TFP) process for a local reinforcement on an "open-hole" tension plate from carbon/epoxy laminates.* Composites Science and Technology, 2003. **63**(1): pp. 81–88
doi: 10.1016/S0266-3538(02)00178-1

[17] B.C. Kim, K. Potter, and P.M. Weaver, *Continuous tow shearing for manufacturing variable angle tow composites.* Composites Part a-Applied Science and Manufacturing, 2012. **43**(8): pp. 1347–1356
doi: 10.1016/j.compositesa.2012.02.024

[18] H. Haddadpour and Z. Zamani, *Curvilinear fiber optimization tools for aeroelastic design of composite wings.* Journal of Fluids and Structures, 2012. **33**: pp. 180–190
doi: 10.1016/j.jfluidstructs.2012.05.008

[19] B.K. Stanford, C.V. Jutte, and K. Chauncey Wu, *Aeroelastic benefits of tow steering for composite plates.* Composite Structures, 2014. **118**(1): pp. 416-422.
doi: 10.1016/j.compstruct.2014.08.007

[20] O. Stodieck, J.E. Cooper, P.M. Weaver, and P. Kealy, *Optimization of Tow-Steered Composite Wing Laminates for Aeroelastic Tailoring.* AIAA Journal, 2015. **53**(8): pp. 2203-2215.
doi: 10.2514/1.J053599

[21] B.K. Stanford, C.V. Jutte, and C.D. Wieseman, *Trim and Structural Optimization of Subsonic Transport Wings Using Nonconventional Aeroelastic Tailoring.* AIAA Journal, 2016. **54**(1): pp. 293-309.
doi: 10.2514/1.J054244

[22] T.R. Brooks, G. Kennedy, and J. Martins, *High-fidelity Aerostructural Optimization of a High Aspect Ratio Tow-steered Wing*, in *57th AIAA/ASCE/AHS/ASC Structures, Structural Dynamics, and Materials Conference, AIAA SciTech, San Diego, California,* 2016.
doi: 10.2514/6.2016-1179

[23] G. Kenway, G. Kennedy, and J. Martins, *Aerostructural optimization of the Common Research Model configuration*, in *15th AIAA/ISSMO Multidisciplinary Analysis and Optimization Conference, Atlanta, Georgia,* 2014
doi: 10.2514/6.2014-3274

[24] K. Svanberg, *A Class of Globally Convergent Optimization Methods Based on Conservative Convex Separable Approximations.* SIAM Journal on Optimization, 2002. **12**(2): pp. 555-573.
doi: 10.1137/S1052623499362822

[25] J. Vassberg, M. DeHaan, S. Rivers, and R. Wahls, *Development of a Common Research Model for Applied CFD Validation Studies*, in *AIAA Applied Aerodynamics Conference*. Honolulu, Hawaii.
doi: 10.2514/6.2008-6919

[26] *Common Research Model Wingbox Finite Element Models*. Access Date: 21/03/2016; Available from: http://commonresearchmodel.larc.nasa.gov

[27] MSC, *NASTRAN*. 2012, MSC.Software; Available from:
http://www.mscsoftware.com/product/msc-nastran

[28] C. G. Broyden, *A class of methods for solving nonlinear simultaneous equations*, Mathematics of Computation, 1965. **19** pp. 577-593
doi: 10.1090/S0025-5718-1965-0198670-6

[29] *Certification Specifications and Acceptable Means of Compliance for Large Aeroplanes (CS-25), Amendment 17,* European Aviation Safety Agency.

[30] W. Mallik, R.K. Kapania, and J.A. Schetz, *Aeroelastic Applications of a Variable-Geometry Raked Wingtip*, Journal of Aircraft, 2016. published online 13 Jun. 2016.
doi: 10.2514/1.C033805

[31] S. Setoodeh, A. Blom, M. Abdalla, and Z. Gürdal, *Generating Curvilinear Fiber Paths from Lamination Parameters Distribution*, in *47th AIAA/ASME/ASCE/AHS/ASC Structures, Structural Dynamics, and Materials Conference*, Newport, Rhode Island, 2006
doi: 10.2514/6.2006-1875

[32] G. Raju, Z. Wu, and P. Weaver, *On Further Developments of Feasible Region of Lamination Parameters for Symmetric Composite Laminates*, in *55th AIAA/ASMe/ASCE/AHS/SC Structures, Structural Dynamics, and Materials Conference*, National Harbor, Maryland, 2014
doi: 10.2514/6.2014-1374

[33] S. Guo, J. De Los Monteros, and Y. Liu, *Gust Alleviation of a Large Aircraft with a Passive Twist Wingtip.* Aerospace, 2015. **2**(2): pp. 135-154
doi: 10.3390/aerospace2020135

[34] S. Adali, *Lay-up optimization of laminated plates under buckling loads*, in *Buckling and Postbuckling of Composite Plates*, G.J. Turvey and I.H. Marshall, Editors. 1995, Springer Netherlands: Dordrecht. pp. 329-365.
doi: 10.1007/978-94-011-1228-4_10

[35] O. Stodieck, J.E. Cooper, and P.M. Weaver, *Interpretation of Bending/Torsion Coupling for Swept, Nonhomogenous Wings.* Journal of Aircraft, 2016. **53**(4): pp. 892-899.
doi: 10.2514/1.C033186

[36] C. Niu, *Airframe structural design practical design information and data on aircraft structures*. 1999, Conmilit Press Ltd.,: Hong Kong. p. 251.